Proceedings of the ASME 2010 International Design Engineering Technical Conferences & Computers and Information in Engineering Conference
IDETC/CIE 2010
August 15-18, 2010, Montreal, Quebec, Canada

DETC2010-29060

MULTI-SUBSTRATE BURROWING PERFORMANCE AND CONSTITUTIVE MODELING OF ROBOCLAM: A BIOMIMETIC ROBOT BASED ON RAZOR CLAMS

Amos G. Winter, V
Hatsopolous Microfluids Laboratory
Precision Engineering Research Group
Massachusetts Institute of Technology
Cambridge, MA 02139
Email: awinter@mit.edu

Robin L.H. Deits
Hatsopolous Microfluids Laboratory
Massachusetts Institute of Technology
Cambridge, MA 02139
Email: robin.deits@gmail.com

Daniel S. Dorsch
Hatsopolous Microfluids Laboratory
Massachusetts Institute of Technology
Cambridge, MA 02139
Email: dorsch@mit.edu

A.E. Hosoi*
Hatsopolous Microfluids Laboratory
Massachusetts Institute of Technology
Cambridge, MA 02139
Email: peko@mit.edu

Alexander H. Slocum
Precision Engineering Research Group
Massachusetts Institute of Technology
Cambridge, MA 02139
Email: slocum@mit.edu

ABSTRACT

The Atlantic razor clam (Ensis directus) reduces burrowing drag by using motions of its shell to fluidize a thin layer of substrate around its body. We have developed RoboClam, a robot that digs using the same mechanisms as Ensis, to explore how localized fluidization burrowing can be extended to engineering applications. In this work we present burrowing performance results of RoboClam in two distinctly different substrates: ideally granular 1mm soda lime glass beads and cohesive ocean mudflat soil. Using a genetic algorithm to optimize RoboClam's kinematics, the machine was able to burrow in both substrates with a power law relationship between digging energy and depth of n = 1.17. Pushing through static soil has a theoretical energy-depth power law of n = 2, which means that Ensis-inspired burrowing motions can provide exponentially higher energy efficiency. We propose a theoretical constitutive model that describes how a fluidized region should form around a contracting body in virtually any type of saturated soil. The model predicts fluidization to be a relatively local effect, extending only two to three characteristic lengths away from the body, depending on friction angle and coefficient of lateral earth pressure, two commonly measured soil parameters.

INTRODUCTION

The motivation behind our work is to generate compact, lightweight, low-energy, reversible, and dynamic burrowing systems for use in subsea applications such as anchoring, oil recovery, mine detonation, and sensor placement. As many organisms have evolved to embed themselves into undersea substrates [1-11], our hypothesis is that nature has found an optimized solution to subsea burrowing. We identified the Atlantic razor clam, *Ensis directus,* as the best candidate for biomimicry because of its performance and engineering merits [2, 10, 11]. *Ensis* burrows at nearly 1cm/s to 70cm deep using approximately 0.21J/cm, which equates to being able to travel over a half kilometer on the energy in a AA battery [12]. Furthermore, razor clams are the size scale of a real engineering device (3.2cm diameter, 16cm long) and are packaged in a rigid shell with only one degree-of-freedom movement. Using the animal's performance and geometry, we have calculated that an *Ensis*-based burrowing/anchoring system would provide a 10X improvement over the best currently available anchoring technology, leading most by more than two orders of magnitude, in anchoring force developed per unit energy expended [13-15].

The burrowing cycle of a razor clam is shown in Fig. 1a-f. b) The animal starts with its foot - a soft, flexible organ - fully extended below the shell. Next, it uses a series of four shell motions to make downward progress: c) the foot extends to uplift the shell; d) the shell halves contract to force blood into

* Address all correspondence to this author

the foot, inflating it to serve as an anchor; e) the foot muscles contract to pull the shell downwards; and f) the shell expands in order to begin the cycle again. To understand the soil mechanics during this cycle, we developed an experimental setup to visualize a razor clam burrowing in 1mm soda lime glass beads, which are similar in size and density to coarse sand [16]. A video of *Ensis* burrowing in our setup can be seen here [17]. Substrate deformation was tracked using particle image velocimetry (PIV) [18]. We discovered that the uplift and contraction movements of the shell draw water towards the animal's body, unpacking and fluidizing the surrounding substrate. Moving through fluidized, rather than packed soil, reduces the amount of energy to reach full burrow depth by nearly three orders of magnitude [19]. Furthermore, because *Ensis* moves through a fluidized medium, the drag force on its body should ideally remain constant with depth. In contrast, moving through a packed, static particulate medium requires pushing force that increases linearly with depth [20]. This means *Ensis* exponentially reduces burrowing energy from scaling with depth squared to linearly increasing with depth.

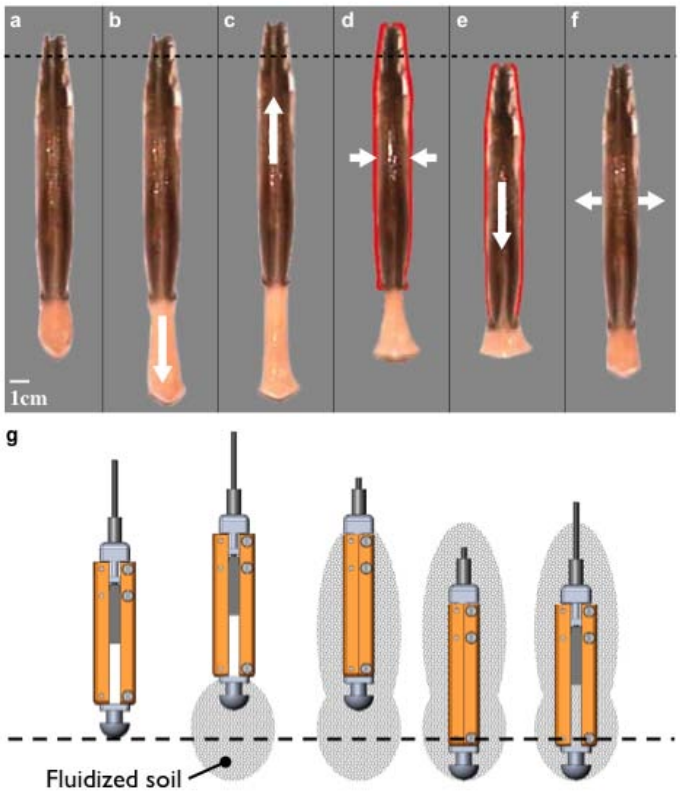

Figure 1 RAZOR CLAM AND ROBOCLAM MOTION. a-f) Razor clam shell motions during a digging cycle. g) Razor clam shell kinematics mimicked by RoboClam end effector. Uplift and contraction movements locally fluidize soil around the end effector, reducing burrowing drag.

To verify that localized fluidization drag reduction could be transferred to engineering burrowing applications, we developed RoboClam, a robot that replicates *Ensis* digging kinematics, which is shown in Fig. 2. RoboClam was designed to yield insight into the relationships between environmental and engineering parameters, such as substrate type, depth, device size, burrowing velocity, and required power. Figure 1g shows the end effector of RoboClam – the part of the robot that digs by mimicking *Ensis* shell motions to locally fluidize the surrounding substrate – going through its burrowing cycle. In RoboClam, *Ensis'* foot has been replaced by a pneumatic piston that pushes down on the end effector, as we have found from our experiments that only *Ensis'* shell motions contribute to localized fluidization.

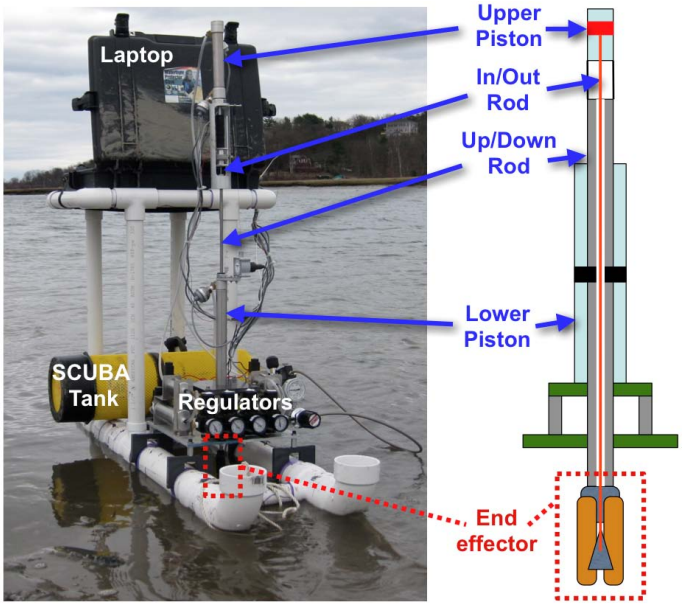

Figure 2 ROBOCLAM BURROWING IN A MUD FLAT WITH SCHEMATIC OF THE MACHINE. RoboClam is composed of two pneumatic pistons, each of which actuates one degree of freedom of the end effector. The lower piston moves the entire end effector up and down. The upper piston actuates the shells of the end effector in and out via a wedge linkage connected to a rod that passes through the lower piston. A laptop controls the machine by turning on and off solenoid valves connected to the pistons. Pressurized air is sourced from a SCUBA tank and regulated for each piston port.

A requirement of RoboClam was that it could be tested in real marine substrates, as to avoid wall effects caused by a container, and to capture the peculiarities of real soil with heterogeneous composition and the presence of organic matter. Figure 2 shows RoboClam burrowing in real *Ensis* habitat off Gloucester, MA. For saltwater compatibility, RoboClam's main power source is an 80 ft^3 scuba tank. Small lead acid batteries power four solenoid valves and digital pressure regulators that direct air to two pneumatic pistons, which control the end effector's two degrees of freedom. A laptop controls the robot

using a genetic algorithm [21], which varies the timescale and pushing force of each of the four end effector movements to find the lowest burrowing 'fitness.' The fitness value in our experiments is the product of the energy expended per unit depth and the exponent of the energy-depth power law relationship. This product was chosen as the fitness value since optimizing one of the parameters alone often resulted in undesirable values of the other.

ROBOCLAM DIGGING PERFORMANCE

RoboClam has been tested in two substrates: 1mm soda lime glass beads and real ocean mud flats off the coast of Gloucester, MA. The former is an idealized granular material, with uniform grains (both in shape and size), high permeability, and no cohesion. The latter is a cohesive sand and silt mixture with low permeability and entrained organic material. Figure 3 shows burrowing data corresponding to the lowest fitness value from testing in both substrates. In all tests the substrates were fully saturated with water. Interestingly, RoboClam was able to burrow with an energy vs depth power law slope of n = 1.17 in both soils, even though they are disparate.

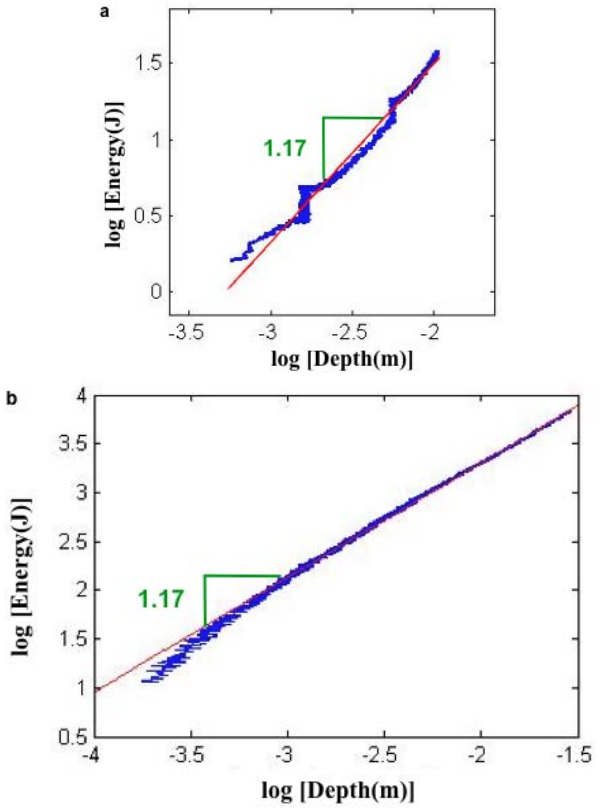

Figure 3 ROBOCLAM MINIMUM FITNESS BURROWING RESULTS IN TWO SUBSTRATES. a) Power law relationship between digging energy and depth while burrowing in saturated 1mm soda lime glass beads. b) Power law relationship between digging energy and depth while burrowing in ocean mud flats off Gloucester, MA.

Not only does n = 1.17 constitute enormous energetic savings over simply pushing through static soil (which theoretically has n = 2), but these data indicate that *Ensis*-inspired burrowing may work in a wide variety of substrates. The remainder of this paper is focused on describing a theoretical model that shows how localized fluidization burrowing should be feasible in virtually any type of particulate substrate.

THEORETICAL PREDICTION OF LOCALIZED FLUIDIZATION

This model describes localized fluidization from the standpoint of *Ensis*. The model is also valid for any other contracting body in a saturated soil, including RoboClam's end effector.

Inertial Effects During Contraction

As a razor clam contracts its shell, it pulls water through the substrate towards its body, causing the adjacent soil particles to separate and fluidize. To determine whether inertial effects are important in this process, the characteristic time scale for the velocity of a soil particle to reach the fluid velocity can be calculated using Stokes drag [22] and conservation of momentum, as shown in Eq. (1).

$$F_D = 6\pi\mu D(V_f - V_p) = \frac{\partial P}{\partial t} \tag{1}$$

F_D is the drag force on the particle, μ is the viscosity of the fluid, D is the diameter of the particle, V_f is the fluid velocity, V_p is the particle velocity, P is the momentum of the particle, and t is time. Substituting in the particle density, ρ_p, and dimensions yields Eq. (2), the differential equation of motion for the particle.

$$\frac{dV}{dt} = \frac{36\mu(V_f - V_p)}{D^2\rho_p} \tag{2}$$

Eq. (2) can be integrated with the variable substitution

$$\xi = V_f - V_p, \quad d\xi = -dV_p$$

Applying t_o = 0 results in Eq. (3)

$$V_p = V_f - \exp\left(\frac{-36\mu t}{D^2\rho_p}\right) \tag{3}$$

with a time constant

$$\tau = \frac{D^2 \rho_p}{36 \mu t}$$

The 1mm soda lime glass beads and water used in our experiments have a characteristic time scale of 0.075s, which is an order of magnitude less than the time scales associated with the clam's movements. Smaller particles, such as in the mudflat soil, will have even smaller characteristic time scales. This means that in the regions where particles are able to move, the fluid and particles will move together as a bulk liquid.

Soil Stress Distribution During Contraction

When the razor clam contracts, it reduces the pressure acting between its shell and the soil, causing the soil to fail. This scenario can be modeled as a cylinder with a contracting radius that is embedded in saturated soil, as shown in Fig. 4.

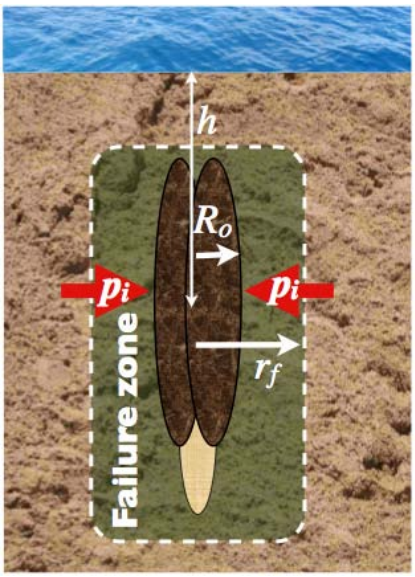

Figure 4 MODEL OF SOIL FAILURE AROUND A CONTRACTING RAZOR CLAM. As a razor clam contracts its shell, it reduces pressure, p_i, against the adjacent soil, causing the soil to fail. The failure model presented in this paper predicts the size of the failure zone as a function of soil properties.

To neglect end effects, the clam is modeled as an infinitely long cylinder. If the relaxation in pressure between the clam's shell and the surrounding soil is considered quasi-static (at incipient failure there is no movement of the fluid and soil particles), stresses due to inertial effects can be ignored and the radial and circumferential stress distribution can be described with the thick-walled pressure vessel equations in Eq. (4) [23].

$$\sigma_r = \frac{a^2 b^2 (p_o - p_i)}{b^2 - a^2} \frac{1}{r^2} + \frac{p_i a^2 - p_o b^2}{b^2 - a^2}$$
$$\sigma_\theta = -\frac{a^2 b^2 (p_o - p_i)}{b^2 - a^2} \frac{1}{r^2} + \frac{p_i a^2 - p_o b^2}{b^2 - a^2} \quad (4)$$

In Eq. (4), σ_r is radial stress, σ_θ is hoop stress, a is the inner radius, b is the outer radius, p_i is the inner pressure, and p_o is the outer pressure. A positive pressure exerts a compressive load, and a compressive stress is negative. It is important to note that these equations still hold if there is a body force acting in the z-direction, such as in a soil. In this case the pressure vessel equations describe the state of stress within annular differential elements stacked in the z-direction.

If the clam is considered to be in an infinite bed of soil in lateral directions, b can be considered infinite. Applying this condition and reversing signs to geotechnical conventions (with compressive stresses positive) results in Eq. (5), which describes the full state of stress in the soil around the clam.

$$\sigma_r = \frac{R_o^{\,2} (p_i - p_o)}{r^2} + p_o$$
$$\sigma_\theta = -\frac{R_o^{\,2} (p_i - p_o)}{r^2} + p_o \quad (5)$$
$$\sigma_z = \rho_t g h$$
$$\tau_{r\theta} = \tau_{\theta z} = 0 \text{ because of symmetry}$$
$$\tau_{rz} = 0 \text{ because of infinitly long clam}$$

In Eq. (5), R_o is the clam's initial radius, h is the clam's depth beneath the surface of the soil, p_i is the pressure between the shell and the soil, and ρ_t is the total density of the soil/fluid mixture. The pressure p_o is the total lateral earth pressure at an infinite distance away from the clam. This pressure minus the pore fluid pressure, u, yields the undisturbed horizontal effective stress

$$\sigma'_{h_o} = p_o - u$$

which is the stress acting between soil particles. The undisturbed horizontal and vertical effective stresses can be correlated through the coefficient of lateral earth pressure (also called coefficient of earth pressure at rest, coefficient of lateral stress, or lateral stress ratio)

$$K_o = \frac{\sigma'_{h_o}}{\sigma'_{v_o}}$$

which is a measured soil property [16, 24]. By also knowing the void fraction of the soil, ε, and the particle and fluid density, p_o can be determined with Eq. (6).

$$\begin{aligned} p_o &= \sigma'_{h_o} + u \\ p_o &= K_o \sigma'_{v_o} + u \\ p_o &= K_o g h (1-\varepsilon)(\rho_p - \rho_f) + \rho_f g h \end{aligned} \tag{6}$$

Failure of the substrate will occur when p_i is lowered to a point where the imbalance of two principle effective stresses produces a shear stress that exceeds the shear strength of the soil. The stress imbalance induced by a contracting cylinder in soil can cause failure in one of two ways: an imbalance between radial and vertical stresses or an imbalance between radial and hoop stresses. These two failure conditions are represented by the Mohr's circle in Fig. 1. The friction angle, φ is a measured property of the soil that depends on composition and packing.

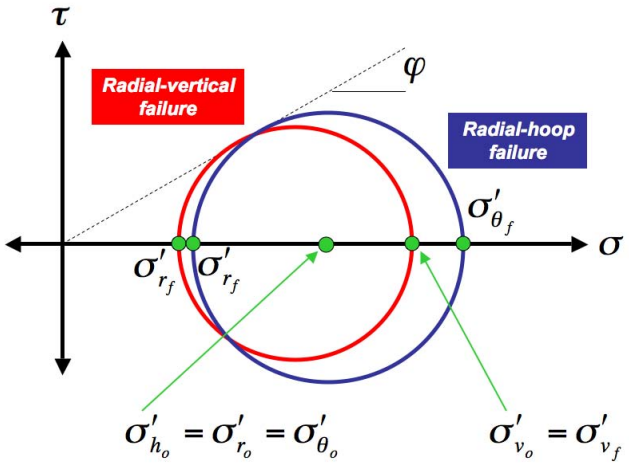

Figure 5 FAILURE STATES IN SOIL. Mohr circle representing failure states in a granular soil due to radial-vertical stress imbalance and radial-hoop stress imbalance. Stresses: τ for shear, σ for normal. Subscripts: *h* for horizontal, *v* for vertical, *r* for radial, θ for hoop, *o* for undisturbed state, *f* for failure state.

A point to make about this failure analysis is that it is also valid for cohesive soils. The one difference is that the failure envelope in a cohesive soil does not pass through 0,0 on a Mohr's circle, as cohesive stresses give soil shear strength even when no compressive stresses are applied. At sufficient depths compressive stresses will dominate cohesive stresses, so a failure envelope for a cohesive soil that runs through 0,0 can be approximated for this condition.

From the geometry of the circle and the failure envelope defined by the friction angel, the relationship between the effective horizontal and vertical stress at failure can be derived, which is represented in Eq. (7), where K_a is called the coefficient of active failure.

$$\left.\frac{\sigma'_{r_f}}{\sigma'_{v_f}}\right|_{rad-vert} = \left.\frac{\sigma'_{r_f}}{\sigma'_{\theta_f}}\right|_{rad-hoop} = \left(\frac{1-\sin\varphi}{1+\sin\varphi}\right) = K_a \tag{7}$$

Combining the radial stress in Eq. (5) with Eqns. (6) and (7) produces Eq. (8), which is an expression for the location of the failure surface, r_f, in the soil surrounding a contracting cylinder when the stress imbalance that causes failure is between radial and vertical stresses.

$$\text{Failure when}: \sigma'_r = \left.\sigma'_{r_f}\right|_{rad-vert}$$

$$\sigma'_r = \sigma_r - u = \left.\sigma'_{r_f}\right|_{rad-vert} = K_a \sigma'_{v_o} = \frac{K_a}{K_o}\sigma'_{h_o} = \frac{K_a}{K_o}(p_o - u)$$

$$\frac{R_o^2(p_i - p_o)}{r^2} + p_o - u = \frac{K_a}{K_o}(p_o - u) \tag{8}$$

$$\Rightarrow \left.\frac{r_f}{R_o}\right|_{rad-vert} = \left(\frac{(p_i - p_o)}{\left(\frac{K_a}{K_o} - 1\right)(p_o - u)}\right)^{1/2}$$

Using a similar process, combining the radial and hoop stresses in Eq. (5) with Eqns. (6) and (7) produces Eq. (9), which is an expression for the location of the failure surface, r_f, due to an imbalance between radial and hoop stresses.

$$\text{Failure when}: \left.\sigma'_{r_f}\right|_{rad-hoop} = K_a \sigma'_{\theta_f}$$

$$\left.\sigma'_{r_f}\right|_{rad-hoop} = \sigma_r - u = K_a \sigma'_{\theta_f} = K_a(\sigma_\theta - u)$$

$$\frac{R_o^2(p_i - p_o)}{r^2} + p_o - u = K_a\left(-\frac{R_o^2(p_i - p_o)}{r^2} + p_o - u\right) \tag{9}$$

$$\Rightarrow \left.\frac{r_f}{R_o}\right|_{rad-hoop} = \left(\frac{(K_a+1)(p_i - p_o)}{(K_a - 1)(p_o - u)}\right)^{1/2}$$

The dominant failure mechanism in the soil surrounding a contracting cylindrical body is determined by the type of failure (radial-vertical or radial-hoop) that results in the largest failure surface radius. This can be calculated by combining Eqns. (8) and (9) into Eq. (10).

$$\frac{r_f\big|_{rad-vert}}{r_f\big|_{rad-hoop}} = \left(\frac{(K_a - 1)}{(K_a + 1)\left(\frac{K_a}{K_o} - 1\right)} \right)^{1/2} \qquad (10)$$

Figure 6 shows Eq. (10) plotted for K_a = 0.19 to 0.52 and K_o = 0.31 to 1, the maximum range of realistic values [16, 24]. Areas greater than one in Fig. 6 indicate the failure surface radius is determined by the imbalance between radial and vertical stresses. Areas less than one indicate the failure surface radius is determined by the imbalance between radial and hoop stresses.

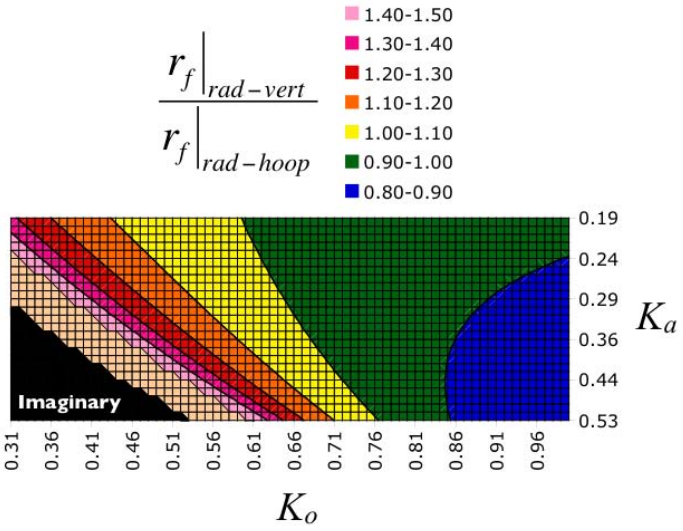

Figure 6 PREDICTION OF DOMINANT FAILURE MECHANISM. Radial-vertical stress induced failure denoted by regions greater than one. Radial-hoop stress induced failure denoted by regions less than one. For most values of K_o and K_a, failure induced by both mechanisms occurs at approximately the same radius.

Figure 6 shows that the failure surface radius predicted by both failure modes will be at approximately the same location for most values of K_a and K_o. As such, either Eq. (8) or (9) can be used to predict the location of the failure surface as a function of soil properties.

Figure 7 shows Eq. (8) plotted vs. depth and internal pressure. When p_i is positive and much lower than p_o, $r_f/R_o \approx 3.2$. When p_i and p_o are on the same order, $r_f/R_o \approx 1.7$. For a wide range of soil properties, the maximum r_f/R_o varies between two and three. These results demonstrate that soil failure around a contracting clam is a relatively local effect, and for large imbalances between p_i and p_o, depth independent.

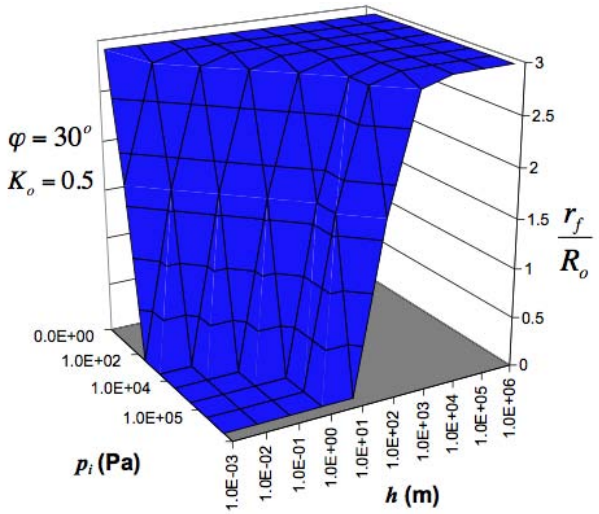

Figure 7 LOCATION OF FAILURE SURFACE OF SOIL AROUND A CONTRACTING CLAM. The plot shows that for a large range of depths and contact pressures between the clam and soil, the failure surface occurs at approximately three clam radii away. This plot is particular to soil with given friction angle and coefficient of lateral earth pressure, which are in the range of common soils.

If during contraction p_i is assumed to be approximately zero, Eq. (8) can be simplified to Eq. (11). This equation is extremely useful, as it facilitates a prediction of the failure surface radius with only two soil properties, K_a and K_o, both of which would be measured in a geotechnical survey.

$$\frac{r_f}{R_o} \approx (K_o - K_a)^{-1/2} \approx 2 \text{ to } 3 \qquad (11)$$

Our hypothesis is that the failure surface bounds the fluidized region. After the contracting body induces failure in the soil, further contraction will draw water into the failed region. Since the particles are essentially inertialess, as shown in section 3.1, they will freely move with the water drawn towards the contracting body. The water will mix with the failed soil to produce fluidized substrate, which provides much less resistance to downward movement than the surrounding packed soil.

CONCLUSIONS AND FUTURE WORK

Two exciting conclusions can be drawn from the work presented in this paper. First, we have shown that RoboClam is able to achieve exponential burrowing energy reductions in two disparate soils: ideally granular soda lime glass beads and real ocean mud flats. The energy-depth power law relationship of n = 1.17 is extremely close to the ideal value of n = 1 predicted for real *Ensis*. Our assumption is that localized fluidization around RoboClam's end effector, as observed during *Ensis* burrowing, is the cause of the measured energetic reductions.

The second conclusion is that the fluidized zone can be predicted using only K_a and K_o, two soil parameters normally measured in a geotechnical survey. Furthermore, the size of the fluidized zone changes little with soil properties, and is relatively depth independent. This means that an *Ensis*-inspired burrowing device may not have to adjust its kinematics for different types of soils and depths, making it flexible for various environments and applications.

We are currently working on 3D visualization of RoboClam burrowing, as to see the size and shape of the fluidized region and verify our theoretical model. We are also testing larger RoboClam end effectors to judge the effect of device size on burrowing performance. Our aim is to assemble experimental and theoretical results into a set of design rules that enable engineers to build locally fluidizing burrowers for any size, soil type, and application.

ACKNOWLEDGMENTS

This work was sponsored by the Battelle Memorial Institute of Columbus, OH, Bluefin Robotics of Cambridge, MA, and Chevron of Houston, TX.

REFERENCES

1. Fager, E.W., *Marine Sediments: Effects of a Tube-Building Polychaete.* Science, 1964. **143**(3604): p. 356-359.
2. Holland, A.F. and J.M. Dean, *Biology of Stout Razor Clam Tagelus-Plebeius .1. Animal-Sediment Relationships, Feeding Mechanism, and Community Biology.* Chesapeake Science, 1977. **18**(1): p. 58-66.
3. Aoyama, J., et al., *First observations of the burrows of Anguilla japonica.* Journal of Fish Biology, 2005. **67**(6): p. 1534-1543.
4. Kelly, M.D., et al., *Burrow extension by crack propagation.* Nature, 2005. **433**(7025): p. 475.
5. Rosenberg, R. and K. Ringdahl, *Quantification of biogenic 3-D structures in marine sediments.* Journal of Experimental Marine Biology and Ecology, 2005. **326**(1): p. 67-76.
6. Shin, P.K.S., A.W.M. Ng, and R.Y.H. Cheung, *Burrowing responses of the short-neck clam Ruditapes philippinarum to sediment contaminants.* Marine Pollution Bulletin, 2002. **45**(1-12): p. 133-139.
7. Stanley, S.M., *Bivalve Mollusk Burrowing Aided by Discordant Shell Ornamentation.* Science, 1969. **166**(3905): p. 634-635.
8. Trueman, E.R., *Bivalve Mollusks: Fluid Dynamics of Burrowing.* Science, 1966. **152**(3721): p. 523-525.
9. Trueman, E.R., *The Dynamics of Burrowing in Ensis (Bivalvia).* Proceedings of the Royal Society of London. Series B, Biological Sciences, 1967. **166**(1005): p. 459-476.
10. Trueman, E.R., *The locomotion of soft-bodied animals*. 1975, London: Edward Arnold.
11. Trueman, E.R., A.R. Brand, and P. Davis, *The Dynamics of Burrowing of Some Common Littoral Bivalves*. J Exp Biol, 1966. **44**(3): p. 469-492.
12. Energizer. *Energizer E91 AA Battery Product Datasheet*. 2009. http://data.energizer.com/PDFs/E91.pdf.
13. Hinz, E.R., *The complete book of anchoring and mooring*. 1 ed. 1986, Centreville, Md: Cornell Maritime Press.
14. McCormick, M.E., *Anchoring systems*. 1 ed. 1979, New York: Pergamon Press.
15. Chance, A.B., *Design Methodology: Chance Helical Anchor/Pile Bearing Capacity*. 2006, Hubbell Power Systems.
16. Lambe, T.W. and R.V. Whitman, *Soil Mechanics*. 1969, New York: John Wiley & Sons.
17. Winter, A., *Video of burrowing Ensis*. 2008.
18. Sveen, J.K., *MatPIV*. 2004. http://folk.uio.no/jks/matpiv/
19. Amos G. Winter, V. *Drag reduction mechanisms employed by burrowing razor clams (Ensis directus)* in *APS DFD*. 2008. San Antonio, TX.
20. Robertson, P.K. and R.G. Campanella, *Interpretation of cone penetration tests. Part I: Sand.* Canadian Geotechnical Journal, 1983: p. 718-733.
21. RL Haupt, S.H., *Practical Genetic Algorithms*. 2004, Hoboken, NJ: John Wiley & Sons, Inc.
22. Kundu, P.K. and I.M. Cohen, *Fluid Mechanics*. 3 ed. 2004, Amsterdam: Elsevier.
23. Timoshenko, S.P., *Theory of Elasticity*. 3rd ed. 1970: McGraw Hill.
24. K Terzaghi, R.P., G Mesri, *Soil Mechanics*. 3rd ed. 1996, New York: John Wiley & Sons.